analytical chemistry

pubs.acs.org/ac Article

Rapid and Sensitive Detection of Nanomolecules by an AC Electrothermal Flow Facilitated Impedance Immunosensor

Anil Koklu,* Jason Giuliani, Carlos Monton, and Ali Beskok

Cite This: *Anal. Chem.* 2020, 92, 7762−7769 Read Online

ACCESS | Metrics & More | Article Recommendations | Supporting Information

ABSTRACT: Conventional immunosensors typically rely on passive diffusion dominated transport of analytes for binding reaction and hence, it is limited by low sensitivity and long detection times. We report a simple and efficient impedance sensing method that can be utilized to overcome both sensitivity and diffusion limitations of immunosensors. This method incorporates the structural advantage of nanorod-covered interdigitated electrodes and the microstirring effect of AC electrothermal flow (ACET) with impedance spectroscopy. ACET flow induced by a biased AC electric field can rapidly convect the analyte onto nanorod structured electrodes within a few seconds and enriches the number of binding molecules because of the excessive effective surface area. We performed numerical simulations to investigate the effect of ACET flow on the biosensor performance. The results indicated that AC bias to the side electrodes could induce fast convective flow, which facilitates the transport of the target molecules to the binding region located in the middle as a floating electrode. The temperature rise due to the Joule heating effect was measured using a thermoreflectance imaging method to find the optimum device operation conditions. The change of impedance caused by the receptors−target molecules binding at the sample/electrode interface was experimentally measured and quantified in real-time using the impedance spectroscopy technique. We observed that the impedance sensing method exhibited extremely fast response compared with those under no bias conditions. The measured impedance change can reach saturation in a minute. Compared to the conventional incubation method, the ACET flow enhanced method is faster in its reaction time, and the detection limit can be reduced to 1 ng/mL. In this work, we demonstrate that this sensor technology is promising and reliable for rapid, sensitive, and real-time monitoring of biomolecules in biologically relevant media such as blood, urine, and saliva.

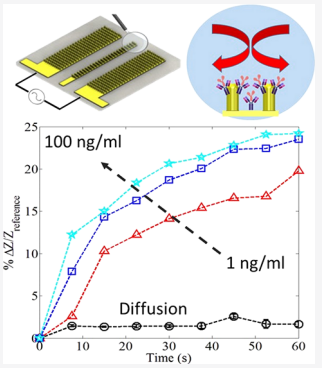

Immunoassays have been widely utilized as powerful and versatile biomedical tools for the diagnosis of certain food toxins,[1,2] environmental pollutants,[3,4] or clinical diseases.[5−9] Because of the specific binding between receptors and target molecules, immunoassays have been broadly used to selectively bind biomolecules that are indicative of the presence of bacteria,[10] viruses,[11] or proteins.[12,13] Conventional immunoassays including the enzyme-linked immunosorbent assay (ELISA) are limited by their portability and high-cost of operation because they rely on fluorescent/enzyme tagging and require sophisticated optical instruments. Recently, microfluidic integrated impedance spectroscopy immunosensors have become a common technique since it provides a label-free, low cost, portable, and sensitive detection for point of care applications.[14−16] In this technique, a small AC voltage is applied to electrodes and, corresponding current and impedance are measured in a wide range of frequencies. For immunosensor applications, target molecule/receptor binding at the electrode surface induces alterations in the impedance, providing a direct means of detection on the sensor. However, the aforementioned techniques rely on receptors/target molecules reactions, which take place through diffusion-dominated transport kinetics. Unfortunately, this mechanism is quite slow, resulting in a long reaction time of several hours and low sensitivity. In extreme cases, these reactions may not even occur. Thus, it is essential to develop a highly sensitive detection method for rapid screening and field-use applications varying from omics (genomics, proteomics) to nanoparticle (CRISPR-Cas9, exosomes, COVID-19) identification.

An effective way for increasing the sensitivity and, at the same time decreasing the response time, can be achieved by generating directional microflows that transport the target molecules toward functionalized sites. Several methods, such as hydrodynamic,[17,18] acoustic,[19,20] and electrokinetic mixing,[21−24] have been employed to increase the reaction rate of receptors/target molecules binding. In the past few years, AC electro-kinetics/dynamics (ACEK-ACED) have been extensively used to manipulate analytes to the detection region.[25−33] All three major ACEK-ACED phenomena, dielectrophoresis (DEP),[34−36] AC electroosmosis (ACEO),[37] and AC electrothermal (ACET),[38] can be used to induce directional biomolecular movement. DEP force is directly applied over

Received: February 27, 2020
Accepted: May 4, 2020
Published: May 4, 2020

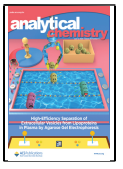

https://dx.doi.org/10.1021/acs.analchem.0c00890
Anal. Chem. 2020, 92, 7762−7769

particles and is proportional to the cube of the target particle diameter. Brownian motion effects increasingly interfere with dielectrophoretic action of nanometer-sized particles, which results in weak attraction/repulsion forces.[39,40] Moreover, DEP forces are short-ranged, and they are typically dominant within a few tens of microns away from the electrodes. It has also been reported that DEP does not work well in highly conductivity media using planar surface electrodes.[41] The ACEO phenomenon typically occurs at low ionic strength, and ACEO flow velocity has been observed to decrease significantly with increasing electrolyte's conductivity and eventually becomes negligible at above 0.1 S/m, making it unsuitable for most bioassays.[42] Our previous studies on AC electrokinetics/electrohydrodynamics revealed that for a biologically relevant high-conductivity media such as phosphate buffer saline (PBS, $\sigma \approx 1.4$ S/m), ACET flow becomes the dominant phenomenon inducing directional and long-range convective vortices which can potentially drag the molecules to the middle of the electrodes' gap, then conveys them tangentially to the electrode surface of the interdigitated electrode pattern.[43,44]

The interdigitated electrode array is a well-known geometric configuration for ACET based microfluidic platforms, as it yields large electric field gradients at small applied potentials. Furthermore, the interdigitated electrode array offers favorable features in terms of low Ohmic drop, the fast establishment of steady-state, and increased signal-to-noise ratio.[45,46] Another important aspect of interdigitated electrodes is that microfluidic system can be designed to develop a robust electronic actuation system to perform a multiplexed protein assay. To carry out the multiplexed functionality, an array of different types of receptors can be patterned along a single microfluidic channel using a pair of addressable asymmetric interdigitated electrodes, where each element is targeting a specific target molecule. By selectively applying voltage at the terminals of each interdigitated electrode pair, ACET flow can assist in transporting the target molecules toward the sensor surface so that the overall binding process can be accelerated. However, planar surface interdigitated electrodes fabricated by conventional photolithography methods have limited effective surface area due to nanosized surface roughness.[24,25,33] Specifically, Cui et al. demonstrated the use of low voltage AC electrothermal effect to enhance and accelerate the detection of low abundance, IgG molecules by AC capacitive sensing with simultaneous ACET enrichment using interdigitated electrodes. After 30 s of measurement, the sensitivities of their device were obtained approximately 0.5%, 4%, and 4% for 1 ng/mL, 10 ng/mL, and 100 ng/mL IgG samples, respectively. 3D nanostructured electrodes can be introduced to enhance sensor sensitivity because they increase the amount of the active binding sites, and consequently, the absorbed volume of target molecules.[47−50] Another fundamental limitation of usage of planar surface electrodes is the onset of electrode polarization (EP) that potentially overwhelms the impedance spectra at the low-frequency range (<10 MHz) depending on electrode size.[51,52] Ions in the electrolyte move toward the electrode surface, leading to a massive interfacial impedance and causing a high-applied voltage drop, which decreases the sensitivity of the measurement. The most effective way to diminish the EP is to enlarge the electrode's effective surface area by depositing nanostructures on the electrode surface.[53−55] Well-ordered nanorod arrays with high density and aspect ratio seem to be the most suitable nanostructures due to their mechanical robustness and electrical stabilities, and it can be fabricated on a large surface area using a template-assisted electrochemical deposition technique in a controllable manner.[56]

The significance of 3D nanostructured surfaces for immunoassay based current sensing was revealed by Lee et al. using a field effect transistor configuration.[57] They utilized carbon nanotube networks decorated with gold nanoparticles, which acted as the actual attaching sites for the probe molecules. The gold nanoparticle decorated carbon nanotube network was fabricated between the island electrode (drain) and enclosing electrode (source) and used as a channel where the antibody/antigen binding takes place and consequently, it changes the current flowing from drain to source. For 100 nM target molecules, they have experimentally shown that the sensitivity of their device was enhanced for the AC biased case (∼23%) compared to the unbiased case (∼16%) after 10 min operation at 1 MHz-5 V condition. However, maintaining a relatively low temperature rise at these operation conditions is a major challenge for high ionic strength solution (1 S/m) since higher conductivity electrolyte are more susceptible to Joule heating effects. Thus, the ACET-induced self-heating must be characterized prior to any electric field excitation to avoid unwanted effects and ensure that ACET is applicable and biologically safe for the required applications. For this purpose, thermoreflectance imaging method was integrated to the fluidic platform to measure the temperature rise at the electrode/electrolyte interface in our previous article. It provides experimental temperature determination in ACET-based microfluidic applications, which allows one to tailor the sensor geometry to keep the Joule heating effects within acceptable ranges for biological samples, or other temperature-sensitive applications.[43]

The hydrophilicity of the sensor surface is a prerequisite for creating a high binding affinity receptor region. In most cases, the surface of the hydrophilic substrate, where the sensors are held, is conjugated with receptors, resulting in low quantities of binding cites on the sensor region. This is due to adhesive forces which cause the receptor assays to spread out over the sensor region.[57] Therefore, localization of the receptors on an electrode surface is the key parameter to fabricate a high-performance immunosensor. This can be achieved by hybrid surfaces at which the electrode surface presents hydrophilic characteristic, while the rest of the substrates remain hydrophobic. Lots of low surface energy materials were selected to modify a hydrophilic surface, such as tridecafluorooctyltriethoxysilane, heptadecafluorodecyl trimethoxysilane, actadecyltrichlorosilane, *n*-octadecanethiol, self-assembly of alkanoic acid through a solution-immersion process, and hexamethyldisilazane (HMDS) as the silylation reagent. A facile, inexpensive, and general approach is explored for the fabrication of transparent hydrophobic surface using HMDS.[58] One unique aspect of HMDS compared with many other passivation layers is that it can react with the surface of SiO_2 or glass to form a self-assembled monolayer and transform the hydrophilic surface to hydrophobic.[59] HMDS can also exhibit a surface roughness comparable to that observed for two-dimensional materials supported by glass substrate.[60] Furthermore, it shows highly biocompatible characteristics which makes it a good candidate for biosensor applications.[61,62]

In this study, we present an effective impedance-based sensing strategy that can significantly enhance speed and sensitivity by combining the structural advantages of nanorod

https://dx.doi.org/10.1021/acs.analchem.0c00890
Anal. Chem. 2020, 92, 7762−7769

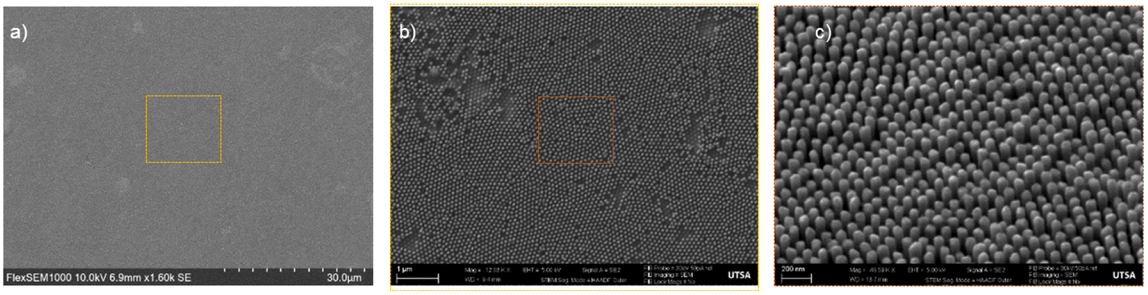

Figure 1. SEM analysis of the nanorod patterned electrodes. Parts (a) and (b) show the top view of the array of nanorods at different magnifications. (c) Tilted view of the nanorods.

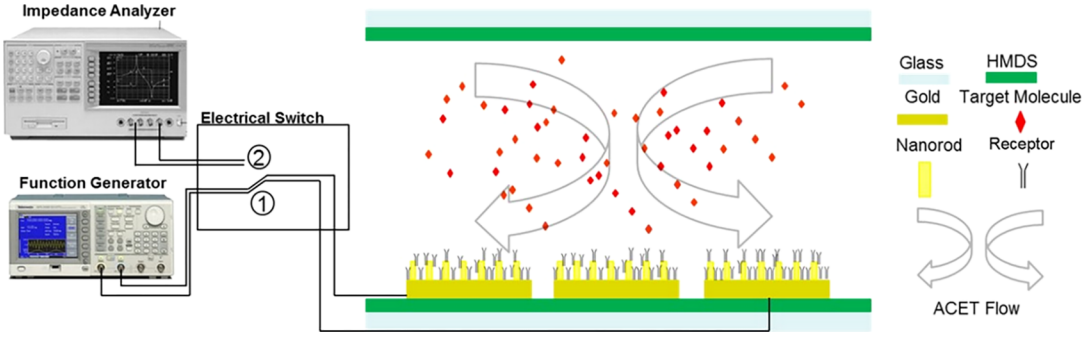

Figure 2. Configuration of the experimental setup. A function generator supplied an AC potential to induce ACET flow to concentrate target molecules onto the receptors-immobilized gold nanorod electrodes, and the binding was then measured using an impedance analyzer for the quantification of the analyte.

electrodes fabricated on a hydrophobic substrate while inducing ACET flow to accelerate the transport of analyte toward the sensing region with immobilized receptors. In this approach, the target molecule level was simultaneously quantified by monitoring the impedance change because of the specific binding of target molecules with receptors. We used numerical simulations to verify that the ACET flow can assist the transport of the target molecules toward the sensor surface so that the overall binding process can be accelerated. Because of the electrokinetic enhancement, the detection sensitivity could be enhanced by at least 1 order of magnitude (compared to the ELISA kit) to reach a nanogram per milliliter (ng mL^{-1}) level, and the detection time could be reduced from several hours to a few seconds. This paper is organized as follows: we first present the sensor fabrication, buffer preparation and sensor surface functionalization, impedance spectroscopy technique, numerical simulations, and the detection mechanism, respectively. Then, experimental results are discussed. Finally, conclusions are presented.

MATERIALS AND METHODS

Sensor Fabrication and Surface Modification. Microfabrication fabrication process is extensively explained in Supporting Information (SI) and summarized in Figure S-1. Briefly, after cleaning the glass substrates, they were vertically dipped into a beaker which was filled with HMDS and acetone solution with 1:1 ratio for various durations. The variation of surface wettability depending on the dipping duration, was explained in SI Figure S-2. Then, the interdigitated electrode array was fabricated on HMDS coated glass substrates using standard photolithography method. The nanopatterning of electrode surfaces was carried out using the template-assisted electrodeposition method, and the details of fabrication were reported in ref 56. A nanoporous anodic aluminum oxide (AAO), which was used as a template, was placed on the planar gold electrode surface and then nickel and gold were sequentially deposited electrochemically through the nanopores (Figure 1a–c). Segmented composition nickel (50 ± 12 nm) /gold (300 ± 12 nm) nanorods were measured using SEM images taken at a 45° inclination at various locations on the electrode. The diameter of the nanorods were determined using a microscopy image segmentation tool (MIST) and is obtained as 102 ± 12 nm. The aspect ratio (height/diameter) of nanorod is calculated as 3.43 which provides self-standing nanorods structures. The tailored nanorods' aspect ratio enables us to maximize the effective receptor/target molecule binding region. After electrochemical deposition, the AAO template was removed in a chromic-phosphoric acid solution at room temperature for 60 min.

Ultra Violet (UV) treatment is an excellent method for increasing the surface hydrophilicity without influencing the electrode microstructure characteristics.[63] The HMDS part of the substrate was covered with a photomask to preserve its hydrophobic behavior, but the electrodes were exposed to UV for 10 min at the power of 110 mJ/cm^2. By doing this, receptors can be selectively coated on the electrode surface which reduces the number of target molecules potentially binding to the other surfaces.

Electrodes with larger sizes were considered to be more cooperative to induce AC electrothermal flow and were successfully used to detect small molecules.[33] Therefore, the device consists of three interdigitated electrodes with 200 μm width and 200 μm spacing. A rectangular portion of the tape was cut using a craft cutter to create a microchannel with 0.4 × 10 × 25 mm^3 (height (H) × width (W) × length (L)) dimensions. The wires used for electrical connections were

https://dx.doi.org/10.1021/acs.analchem.0c00890
Anal. Chem. 2020, 92, 7762−7769

bonded using conductive silver epoxy (MG Chemicals). Another HMDS coated glass slide was used as a cover on the top of the microfluidic channel to increase the flow velocity due to velocity slip on HDMS surfaces and reduce the possibility of target molecules binding. A diamond drill was used to create the fluidic ports, and copper tapes were used for electrical connections.

Buffer Solution Preparation and Electrode Surface Functionalization. PBS ($\sigma \approx 1.4\ S/m$) was prepared by 1:10 volume dilution of physiological strength stock solution with deionized water to obtain 1 mM phosphate buffer (pH 7.0) containing 0.05 v/v% Tween 20 (Fisher Scientific). The sensitivity of the microfluidic sensor was determined by measuring the binding of goat antibovine IgG (H+L) (Jackson ImmunoResearch Laboratories Inc.) (Receptors) to bovine IgG whole molecules (Jackson ImmunoResearch Laboratories Inc.) (Target molecules). Bovine IgG whole molecules were immobilized on the electrodes prior to the test. The microfluidic chip was incubated in an incubator for different time scales ranging from 1 h to 6 h. Different concentrations of the antibovine IgG antibody were loaded at concentrations ranging from 1 to 100 ng/mL in PBS.

Detection Mechanism. The detection mechanism is based on interrogating the impedance change at the interface between a sensor electrode and the sample solution due to the binding reaction. Figure 2 schematically shows the operation mechanism of this sensor. An AC voltage at a certain frequency was applied to the side electrodes using a function generator (Tektronix AFG3102). ACET flow carries the target molecules to the immobilized receptors region and the impedance simultaneously increases due to the chemical binding. Then, impedance measurements were conducted by switching the input from function generator to impedance analyzer (4194A, Agilent) via an electrical switch for every 7.5 s which gives 8 data points for every minute. First, the impedance analyzer was operated at 401 discrete frequencies from 1 kHz to 10 MHz at 20 mV to determine the optimum frequency range for molecule detection. The impedance measurements and equivalent circuit model (Figure S-3) analysis were explained in the SI. The impedance spectra of PBS solution were measured before and after the receptors coating. When the optimum frequency was selected, impedance measurements were performed at a single frequency for the target molecule detection. The impedance of the system spontaneously increases until all the target molecules are trapped on the functionalized site of the electrodes. The binding of target molecules to the receptors can be obtained by calculating the normalized impedance change rate using the following equation,

$$\Delta Z/Z_{\text{reference}} = (Z_{\text{after binding}} - Z_{\text{before binding}})/Z_{\text{before binding}} \quad (1)$$

The calculated $\Delta Z/Z_{\text{reference}}$ was used as an indication of target molecules binding to the antibody.

A theoretical model describing ACET flow facilitated antibody/antigen reaction in microfluidic system was extensively explained in the SI. The model consists of electrostatic, energy, *Stokes*, and first order *Langmuir* adsorption model coupled with transport equations.

RESULTS

Importance of Wettability for Impedance Measurements. Wetting characteristics of the electrodes were investigated utilizing contact angle measurements. Static contact angle measurements were explained in the SI. The baseline glass surface shows a hydrophilic characteristic with a water contact angle of ~19 ± 2.3°. After the surface of the glass was treated for 24 h in HMDS solution, the surface became hydrophobic with a water contact angle of 99° ± 1.7. The change of the wettability characteristic is attributed to the chemistry of the HMDS. Bare glass is hydrophilic because of OH^- termination and water molecules can easily attach to the hydrogen of these silanol groups on the SiO_2 to form a thin water film but HMDS screens water molecules. After coating the glass surface with HMDS for 24 h, gold interdigitated electrodes were fabricated using standard photolithography method described in the sensor fabrication part (Figure S-4a). The contact angle of a water droplet on the gold electrode was measured 77.87° ± 1.54° (Figure S-4b). After 10 min of selectively exposing a UV using mask aligner (MJB-3-Mask Aligner) at the power of 150 W, the water droplet completely infiltrated into the electrode surface, indicating a marked surface transition from hydrophilic to super hydrophilic, resulting in a contact angle less than 10° for planar electrodes (Figure S-4c).

It is well-known that vertically oriented nanorod with the well-faceted (001) shows superhydrophobic characteristics because of high surface roughness and low surface free energy but we could not conduct contact angle measurements due to the small actual electrode area (Figure S-1, red dashed rectangle). However, the hydrophobic behavior of the nanorod structured electrodes can be indirectly assessed by impedance measurements. The impedance measurements were performed with PBS for nanorod and planar electrodes. Each measurement was repeated at least three times, and the average impedance magnitude and phase angles were reported. The normalized standard deviation in all cases was less than 1% and hence, they were not shown in the figure for the sake of clarity. Figure 3 shows the Bode representation of the average

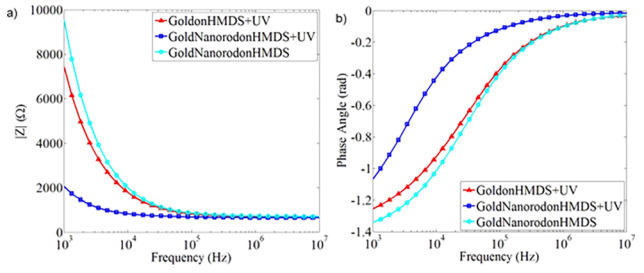

Figure 3. Impedance magnitude (a) and phase angle (b) spectrum of gold planar (red) and gold nanorod structured (dark (After UV treatment) and light blue (Before UV treatment)) electrodes.

impedance spectra of gold planar and nanorod structured electrodes. At frequencies below 1 MHz, the impedance magnitude increased with decreasing frequency, and the phase angle value shifted toward $-\pi/2$ radians. These changes are revealing capacitive charging at the electrode surface because of the EP effect. Since this phenomenon is mainly capacitive (C), it is proportional to the surface area of electrodes. As the effective surface area (A) of the electrode increases with nanorod structures, the magnitude of the impedance should proportionally decrease ($Z \approx 1/C$) but the results were not consistent with the impedance behavior of a capacitor. Nanorod structured surfaces tended to be more hydrophobic,

https://dx.doi.org/10.1021/acs.analchem.0c00890
Anal. Chem. 2020, 92, 7762−7769

leading to poor reaction kinetics between the electrolyte and the electrode and weakening the ionic transport. Bubble pockets can shield the electrode surface which causes a high impedance value. After the nanorod electrode surface was exposed to UV, the impedance magnitude decreased drastically compared to that of measured with a gold planar electrode and the usable frequency bandwidth expanded (Figure 3).

Selection of Sensor Operation Conditions. To ensure good electrical connections and proper impedance behaviors of the electrodes, before the ACET activation, the impedance spectra of the sensor filled with PBS were measured from 1 kHz to 10 MHz with an excitation voltage of 20 mV in the absence of target molecules. In the low-frequency range, EP overshadowed the impedance spectra, and this behavior was diminished about 5 MHz for gold planar electrodes and the impedance magnitude converges a frequency-independent resistive plateau (Figure 3). Therefore, 5 MHz was selected as a critical frequency for the impedance-based sensitivity measurements.

The ACET force expression can be expressed in terms of a directional parameter,

$$M = \left(\left(\frac{T}{\sigma}\frac{\partial\sigma}{\partial T} - \frac{T}{\varepsilon}\frac{\partial\varepsilon}{\partial T}\right)/(1 + (\omega\tau)^2)\right) + 0.5\frac{T}{\varepsilon}\frac{\partial\varepsilon}{\partial T} \quad (2)$$

which is a function of frequency for a fixed type of liquid and temperature (parameters are defined in SI). The amplitude of ACET force can be predicted with M factor, which remains maximum until 10 MHz for 1.4 S/m PBS solution (Figure S-5) and therefore, the side electrodes were also excited at 5 MHz using the function generator. Moreover, most of the AC potential would be applied over the resistive fluid bulk which poses the highest AC electrothermal flow velocities.[43]

The amplitude of applied potential cannot be increased arbitrarily because higher voltages may lead to detachment of the functionalized layer over the electrode surface and lead to malfunction of the sensor due to the Joule heating effect. At high conductivities, temperatures beyond a few degrees ($T >$ 10°C) are likely to occur under an applied AC potential of even a few volts.[64,65] Therefore, the ACET-induced temperature must be measured before any electric field excitation to avoid unwanted effects and ensure that ACET is applicable and biologically safe for the required applications.[24,33,66,67] The temperature rise at the electrodes induced by Joule heating is characterized using the TMX Scientific T°Imager thermoreflectance (TR) imaging system. TR method, which is based on measuring the temperature induced surface reflectance change, is an optical thermal metrology method that is nondestructive, noninvasive, and noncontact. The method employs a lock-in differential measurement that improves its precision, and uses monochromatic light illumination in the visible spectrum, which can provide the spatial resolution to around 0.2−0.5 μm and detect 0.1 K temperature changes. It also does not require special sample preparations, can obtain quick thermal maps, and can optically reach the electrode regions in microchannel. The detail of the measurement technique is explained in ref 43 and the SI. As expected from the Joule heating term, temperature increases with increasing activation voltage, and hence, the temperature rise was measured at different excitation voltages at 5 MHz. The results are given in SI Figure S-6. The temperature rise was obtained less than 10 °C up to 10 V_{pp} and is considered safe for biomicrofluidic applications.

Importance of Wettability for Surface Functionalization. The fast binding reactions were considered between the receptors and electrodes due to the hydrophilicity of the UV exposed electrode surface. After the surface of electrodes was treated with the receptors inside an incubator, it was gently rinsed with PBS and the microfluidic channel was placed by centering the electrodes in the middle. Then, impedance measurements were conducted by pipetting PBS buffer in the microfluidic channel.

After 6 h of incubation process, impedance values have increased from 688.2 Ω (0 h) to 723.4 Ω (6 h) at 5 MHz for UV treated planar gold electrodes, indicating adequate molecular immobilization on the electrode surface. The importance of a hybrid surface to increase the concentration of receptors on the electrode surfaces was evaluated by comparing the impedance spectra measured with the gold planar electrode fabricated on a hydrophilic glass surface. The impedance behavior of PBS measured with an hour incubated gold planar electrode fabricated on the glass surface (1h*) was obtained similar to that of gold electrodes fabricated on HMDS at 0-h incubation. Since the receptor solution spreads out on the glass surface, the concentration of receptors immobilized on the electrode is very low to induce a distinction on the impedance spectra. Then, the same measurements were repeated for UV treated gold nanorod structured electrodes fabricated on HMDS coated glass slides. The impedance spectra are shown in Figure 4c and 4d. First, the impedance magnitude increased from 605.6 Ω to 945.1 Ω at 5 MHz after an hour incubation with the receptors.

The reason for this huge difference can be attributed to the area of the active binding regions, which is increased in the presence of nanorods. The second important point is the saturation of the attached receptors after an hour incubation

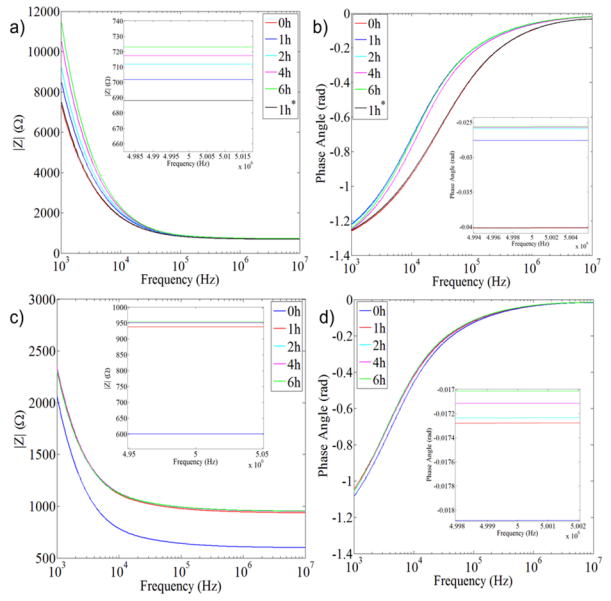

Figure 4. Impedance magnitude (a) and phase angle (b) for gold planar electrode fabricated on HMDS for different antibody incubation times ranging from 0 to 6 h. Black line represents the impedance spectra of receptors incubated on gold electrode fabricated on glass for an hour. Impedance magnitude (c) and phase angle (d) for gold nanorod electrode at different antibody incubation times ranging from 0 to 6 h.

https://dx.doi.org/10.1021/acs.analchem.0c00890
Anal. Chem. 2020, 92, 7762−7769

because the impedance magnitude remained almost the same for the case of 6-h incubation.

Target Molecule Detection. The applied voltage range was determined using the TR method explained in the Selection of Sensor Operation Conditions section but the effect of applied voltage on sensitivity measurements must be investigated by sweeping the voltage from 1 to 10 Vpp. The side electrodes were excited with 180° phase difference for 60 s, and the results are depicted in Figure 5 for UV treated planar and nanorod electrodes. In the absence of ACET flow, the microfluidic devices could not sense the target molecules in a minute because of slow diffusion-based transport ($t_D \approx \frac{L^2}{D} \sim 30$ minutes).

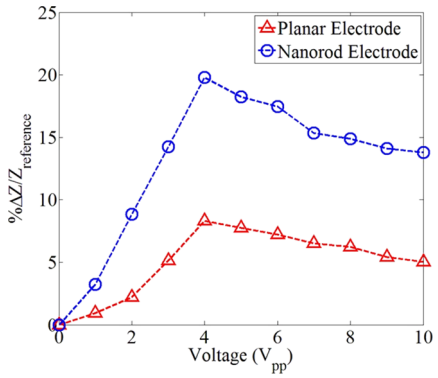

Figure 5. Percentile normalized impedance change with different applied voltages for 1 ng/mL concentration of target molecules mixed PBS solution for 60 s.

Alternatively, they were transmitted onto the sensor region via the circulatory flow and trapped on the receptors. The normalized impedance-change increases until a critical applied voltage (4 V_{pp}), and then it drops to a certain value. The possible reasons are the low residence time of target molecules on receptors or the degradation of receptors due to temperature rise. Although high applied voltages ($F_{ET} \sim V^4$) can induce fast convection flow, which facilitates the transport of the target molecules to the binding region; they could not find enough time to attach to the immobilized receptors. Moreover, temperature rise can potentially cause damage to the receptors which decreases the number of captured target molecules on the sensor.

The specific binding reactions were conducted with Bovine IgG whole molecules by applying a 5 MHz AC voltage at 4 V_{pp} for ACET flow, which increases the temperature by 2 °C on the electrode surface (Figure S-6). Five MHz AC signal at 20 mV was employed as the measuring signal. Electrodes with 6 h of incubated receptors were used for these measurements. The normalized impedance change rates were plotted as a function of time in Figure 6 for planar (Figure 6a) and nanorod structured (Figure 6b) electrodes using three different concentrations of the solution.

As shown in Figure 6, the impedance of the solution without ACET flow remains constant around zero during the test. However, the impedance of the system with ACET flow increases monotonically with time due to the binding reactions. AC biasing led to a significant enhancement of the binding rate compared with that under unbiased conditions. For 100 ng/mL of target solution, the impedance change reached almost 15%/min and 25%/min within 60 s using the planar and nanorod structured electrodes, respectively. The impedance change rates for various dilutions of target molecules are also demonstrated in Figure 6. As expected, when the sample became more diluted, the impedance change decreased to 8%/min and 20%/ for planar and nanorod electrodes. The results in Figure 6 demonstrate that ACET facilitated impedance method is a quantitative method within a detection range of 1 ng/mL of target molecules.

The binding process was also simulated using COMSOL Multiphysics for the same size of device and concentration of molecules to visualize the binding reaction better. Unless the analyte solution is moved toward the sensor surface using an external force, a few microns thick analyte depletion zone forms next to the sensor surface in the solution, which causes poor detection and low sensitivity in biosensing (Figure S-7a). After the side electrodes were excited at 4 V_{pp}, the thickness of the depletion zone was significantly increased, which indicated that the depletion of the target molecules near the sensor surface was suppressed as a result of the continuous supply of the target molecules from the bulk electrolyte (Figure S-7b).

CONCLUSIONS

The electrodes in this work were planar and nanorod structured interdigitated gold electrodes that are fabricated by standard photolithography and template-assisted electrochemical deposition method. Using hybrid surfaces reduces the pumping power and most importantly allows functionalization

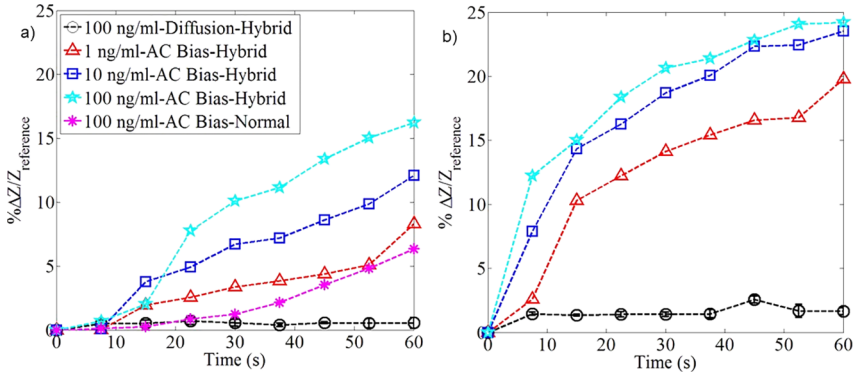

Figure 6. Percentile normalized impedance changes with time for different concentrations of target molecules measured by planar (a) and nanorod (b) electrodes. The ACET flow is generated by applying 5 MHz AC voltage at 4 V_{pp} and 5 MHz AC signal at 20 mV was employed as the measuring signal.

https://dx.doi.org/10.1021/acs.analchem.0c00890
Anal. Chem. 2020, 92, 7762−7769

of the sensor surfaces with antibodies, which not only minimizes the amount of used antibodies but also decreases cross-contamination between distinctly functionalized sensor surfaces. The binding process was aided by AC electrothermal flow that accelerates the transport of target molecules to the electrodes, where the surface was functionalized with receptors and enhance the detection of target molecules. The changes in the impedance at an optimum frequency (5 MHz) were measured every 7.5 s within a minute. The impedance change reached almost 15%/min and 25%/min within 60 s using the planar and nanorod structured electrodes, respectively. The results demonstrate that the ACET enhanced impedance immunosensor allows the directed immobilization of molecules onto microelectrodes at a very low concentration of 1 ng/mL in a significant short time (the 60 s). The ACET flow integrated impedance immunosensors will greatly expand the application scope of electric field driven detection methods in microfluidic chips. In the future, a microfluidic chip with an asymmetric interdigitated electrode array, where each pair of electrode's surface-functionalized with different receptors, will be fabricated and integrated with a robust electronic actuation system to perform as a multiplexed immunosensor. The physiological media will be circulated in a loop utilizing ACET flow, and the change in the impedance due to the binding of target molecules and receptors will be simultaneously monitored for each electrode pair.

■ ASSOCIATED CONTENT

Supporting Information

The Supporting Information is available free of charge at https://pubs.acs.org/doi/10.1021/acs.analchem.0c00890.

Electrode fabrication process, contact angle measurements, impedance spectroscopy measurements, M-factor calculation, temperature rise measurements, theory, and numerical simulations (PDF)

■ AUTHOR INFORMATION

Corresponding Author

Anil Koklu − *Biological and Environmental Science and Engineering, King Abdullah University of Science and Technology (KAUST), Thuwal 23955-6900, Saudi Arabia;* orcid.org/0000-0002-3507-9308; Email: anil.koklu@kaust.edu.sa

Authors

Jason Giuliani − *Department of Physics and Astronomy, University of Texas at San Antonio, San Antonio, Texas 78249, United States*

Carlos Monton − *General Atomics, San Diego, California 92186, United States;* orcid.org/0000-0003-3472-873X

Ali Beskok − *Department of Mechanical Engineering, Southern Methodist University, Dallas, Texas 75205, United States;* orcid.org/0000-0002-8838-5683

Complete contact information is available at: https://pubs.acs.org/10.1021/acs.analchem.0c00890

Notes

The authors declare no competing financial interest.

■ ACKNOWLEDGMENTS

The authors are grateful to Mr. Assaad El Helou and Dr. Peter E. Raad for their assistance in integrating thermoreflectance method to fluidic systems. We are also thankful to SMU Hunt Institute for their support.

■ REFERENCES

(1) Raeisossadati, M. J.; Danesh, N. M.; Borna, F.; Gholamzad, M.; Ramezani, M.; Abnous, K.; Taghdisi, S. M. *Biosens. Bioelectron.* **2016**, *86*, 235−246.

(2) Orlov, A. V.; Khodakova, J. A.; Nikitin, M. P.; Shepelyakovskaya, A. O.; Brovko, F. A.; Laman, A. G.; Grishin, E. V.; Nikitin, P. I. *Anal. Chem.* **2013**, *85* (2), 1154−1163.

(3) Lafleur, J. P.; Senkbeil, S.; Jensen, T. G.; Kutter, J. P. *Lab Chip* **2012**, *12* (22), 4651−4656.

(4) Pol, R.; Céspedes, F.; Gabriel, D.; Baeza, M. *TrAC, Trends Anal. Chem.* **2017**, *95*, 62−68.

(5) Su, W.; Gao, X.; Jiang, L.; Qin, J. *Journal of Chromatography A* **2015**, *1377*, 13−26.

(6) Chen, P.; Chung, M. T.; McHugh, W.; Nidetz, R.; Li, Y.; Fu, J.; Cornell, T. T.; Shanley, T. P.; Kurabayashi, K. *ACS Nano* **2015**, *9* (4), 4173−4181.

(7) Zhu, C.; Yang, G.; Li, H.; Du, D.; Lin, Y. *Anal. Chem.* **2015**, *87* (1), 230−249.

(8) Sechi, D.; Greer, B.; Johnson, J.; Hashemi, N. *Anal. Chem.* **2013**, *85* (22), 10733−10737.

(9) Dou, M.; Dominguez, D. C.; Li, X.; Sanchez, J.; Scott, G. *Anal. Chem.* **2014**, *86* (15), 7978−7986.

(10) Altintas, Z.; Akgun, M.; Kokturk, G.; Uludag, Y. *Biosens. Bioelectron.* **2018**, *100*, 541−548.

(11) Mu, X.; Zhang, L.; Chang, S.; Cui, W.; Zheng, Z. *Anal. Chem.* **2014**, *86* (11), 5338−5344.

(12) Sardesai, N. P.; Kadimisetty, K.; Faria, R.; Rusling, J. F. *Anal. Bioanal. Chem.* **2013**, *405* (11), 3831−3838.

(13) Jeong, S.; Park, J.; Pathania, D.; Castro, C. M.; Weissleder, R.; Lee, H. *ACS Nano* **2016**, *10* (2), 1802−1809.

(14) Xu, M.; Wang, R.; Li, Y. *Talanta* **2016**, *148*, 200−208.

(15) Shin, S. R.; Zhang, Y. S.; Kim, D.-J.; Manbohi, A.; Avci, H.; Silvestri, A.; Aleman, J.; Hu, N.; Kilic, T.; Keung, W.; et al. *Anal. Chem.* **2016**, *88* (20), 10019−10027.

(16) Guo, X.; Kulkarni, A.; Doepke, A.; Halsall, H. B.; Iyer, S.; Heineman, W. R. *Anal. Chem.* **2012**, *84* (1), 241−246.

(17) Mohamadi, R. M.; Besant, J. D.; Mepham, A.; Green, B.; Mahmoudian, L.; Gibbs, T.; Ivanov, I.; Malvea, A.; Stojcic, J.; Allan, A. L.; et al. *Angew. Chem., Int. Ed.* **2015**, *54* (1), 139−143.

(18) Murlidhar, V.; Zeinali, M.; Grabauskiene, S.; Ghannad-Rezaie, M.; Wicha, M. S.; Simeone, D. M.; Ramnath, N.; Reddy, R. M.; Nagrath, S. *Small* **2014**, *10* (23), 4895−4904.

(19) Mao, Z.; Li, P.; Wu, M.; Bachman, H.; Mesyngier, N.; Guo, X.; Liu, S.; Costanzo, F.; Huang, T. J. *ACS Nano* **2017**, *11* (1), 603−612.

(20) Hammarström, B.; Laurell, T.; Nilsson, J. *Lab Chip* **2012**, *12* (21), 4296−4304.

(21) Mirzajani, H.; Cheng, C.; Wu, J.; Chen, J.; Eda, S.; Aghdam, E. N.; Ghavifekr, H. B. *Biosens. Bioelectron.* **2017**, *89*, 1059−1067.

(22) Cheng, I.-F.; Yang, H.-L.; Chung, C.-C.; Chang, H.-C. *Analyst* **2013**, *138* (16), 4656−4662.

(23) Li, S.; Cui, H.; Yuan, Q.; Wu, J.; Wadhwa, A.; Eda, S.; Jiang, H. *Biosens. Bioelectron.* **2014**, *51*, 437−443.

(24) Feldman, H. C.; Sigurdson, M.; Meinhart, C. D. *Lab Chip* **2007**, *7* (11), 1553−1559.

(25) Salari, A.; Thompson, M. *Sens. Actuators, B* **2018**, *255*, 3601−3615.

(26) Ouyang, M.; Mohan, R.; Lu, Y.; Liu, T.; Mach, K. E.; Sin, M. L.; McComb, M.; Joshi, J.; Gau, V.; Wong, P. K.; et al. *Analyst* **2013**, *138* (13), 3660−3666.

(27) Cui, H.; Li, S.; Yuan, Q.; Wadhwa, A.; Eda, S.; Chambers, M.; Ashford, R.; Jiang, H.; Wu, J. *Analyst* **2013**, *138* (23), 7188−7196.

(28) Li, S.; Ren, Y.; Jiang, H. *RSC Adv.* **2014**, *4* (18), 9064−9071.

(29) Liu, X.; Yang, K.; Wadhwa, A.; Eda, S.; Li, S.; Wu, J. *Sens. Actuators, A* **2011**, *171* (2), 406−413.

(30) Hart, R.; Ergezen, E.; Lec, R.; Noh, H. M. *Biosens. Bioelectron.* **2011**, *26* (8), 3391−3397.

(31) Sin, M. L.; Liu, T.; Pyne, J. D.; Gau, V.; Liao, J. C.; Wong, P. K. *Anal. Chem.* **2012**, *84* (6), 2702−2707.
(32) Liu, X.; Cheng, C.; Wu, J.; Eda, S.; Guo, Y. *Biosens. Bioelectron.* **2017**, *90*, 83−90.
(33) Cui, H.; Cheng, C.; Lin, X.; Wu, J.; Chen, J.; Eda, S.; Yuan, Q. *Sens. Actuators, B* **2016**, *226*, 245−253.
(34) Mansoorifar, A.; Koklu, A.; Ma, S.; Raj, G. V.; Beskok, A. *Anal. Chem.* **2018**, *90* (7), 4320−4327.
(35) Fernandez, R. E.; Koklu, A.; Mansoorifar, A.; Beskok, A. *Biomicrofluidics* **2016**, *10* (3), No. 033101.
(36) Mansoorifar, A.; Koklu, A.; Sabuncu, A. C.; Beskok, A. *Electrophoresis* **2017**, *38* (11), 1466−1474.
(37) Song, Y.; Chen, P.; Chung, M. T.; Nidetz, R.; Park, Y.; Liu, Z.; McHugh, W.; Cornell, T. T.; Fu, J.; Kurabayashi, K. *Nano Lett.* **2017**, *17* (4), 2374−2380.
(38) Koklu, A.; Tansel, O.; Oksuzoglu, H.; Sabuncu, A. C. *IET Nanobiotechnol.* **2016**, *10* (2), 54−61.
(39) Castellanos, A.; Ramos, A.; Gonzalez, A.; Green, N. G.; Morgan, H. *J. Phys. D: Appl. Phys.* **2003**, *36* (20), 2584.
(40) Park, S.; Beskok, A. *Anal. Chem.* **2008**, *80* (8), 2832−2841.
(41) Koklu, A.; Sabuncu, A. C.; Beskok, A. *Electrophoresis* **2017**, *38* (11), 1458−1465.
(42) Salari, A.; Navi, M.; Lijnse, T.; Dalton, C. *Micromachines* **2019**, *10* (11), 762.
(43) Koklu, A.; El Helou, A.; Raad, P. E.; Beskok, A. *Anal. Chem.* **2019**, *91* (19), 12492−12500.
(44) Park, S.; Koklu, M.; BeskoK, A. *Anal. Chem.* **2009**, *81* (6), 2303−2310.
(45) Amatore, C.; Fosset, B.; Bartelt, J.; Deakin, M.; Wightman, R. *J. Electroanal. Chem. Interfacial Electrochem.* **1988**, *256* (2), 255−268.
(46) Ciszkowska, M.; Stojek, Z. *J. Electroanal. Chem.* **1999**, *466* (2), 129−143.
(47) Yuan, J.; Wang, K.; Xia, X. *Adv. Funct. Mater.* **2005**, *15* (5), 803−809.
(48) Wei, A.; Sun, X. W.; Wang, J.; Lei, Y.; Cai, X.; Li, C. M.; Dong, Z.; Huang, W. *Appl. Phys. Lett.* **2006**, *89* (12), 123902.
(49) Luo, D.; Wu, L.; Zhi, J. *ACS Nano* **2009**, *3* (8), 2121−2128.
(50) Lee, S.-W.; Lee, K.-S.; Ahn, J.; Lee, J.-J.; Kim, M.-G.; Shin, Y.-B. *ACS Nano* **2011**, *5* (2), 897−904.
(51) Koklu, A.; Ajaev, V.; Beskok, A. *Anal. Chem.* **2019**, *91* (17), 11231−11239.
(52) Koklu, A.; Mansoorifar, A.; Beskok, A. *Electrophoresis* **2019**, *40* (5), 766−775.
(53) Koklu, A.; Sabuncu, A. C.; Beskok, A. *Electrochim. Acta* **2016**, *205*, 215−225.
(54) Koklu, A.; Mansoorifar, A.; Beskok, A. *Anal. Chem.* **2017**, *89* (22), 12533−12540.
(55) Koklu, A.; Mansoorifar, A.; Giuliani, J.; Monton, C.; Beskok, A. *Anal. Chem.* **2019**, *91* (3), 2455−2463.
(56) Guiliani, J.; Cadena, J.; Monton, C. *Nanotechnology* **2018**, *29* (7), No. 075301.
(57) Lee, W. C.; Lee, H.; Lim, J.; Park, Y. J. *Appl. Phys. Lett.* **2016**, *109* (22), 223701.
(58) San Vicente, G.; Bayón, R.; Germán, N.; Morales, A. *Sol. Energy* **2011**, *85* (4), 676−680.
(59) Terpilowski, K.; Goncharuk, O. *Mater. Res. Express* **2018**, *5* (1), No. 016409.
(60) Wang, F.; Wang, X.; Xie, A.; Shen, Y.; Duan, W.; Zhang, Y.; Li, J. *Appl. Phys. A: Mater. Sci. Process.* **2012**, *106* (1), 229−235.
(61) Pecheva, E. In *Study of Biocompatible and Biological Materials: Can They Be Influenced by External Factors?*; Materials Research Forum, LLC, 2017.
(62) Ayibaike, D.; Cui, M.; Wei, J. *Appl. Sci.* **2018**, *8* (11), 2152.
(63) Feng, X.; Feng, L.; Jin, M.; Zhai, J.; Jiang, L.; Zhu, D. *J. Am. Chem. Soc.* **2004**, *126* (1), 62−63.
(64) Ramos, A.; Morgan, H.; Green, N. G.; Castellanos, A. *J. Phys. D: Appl. Phys.* **1998**, *31* (18), 2338.
(65) Green, N. G.; Ramos, A.; Gonzalez, A.; Castellanos, A.; Morgan, H. *J. Electrost.* **2001**, *53* (2), 71−87.
(66) Liu, T.; Sin, M. L.; Pyne, J. D.; Gau, V.; Liao, J. C.; Wong, P. K. *Nanomedicine* **2014**, *10* (1), 159−166.
(67) Chaurey, V.; Polanco, C.; Chou, C.-F.; Swami, N. S. *Biomicrofluidics* **2012**, *6* (1), No. 012806.

https://dx.doi.org/10.1021/acs.analchem.0c00890
Anal. Chem. 2020, 92, 7762−7769